Results in Materials 21 (2024) 100523

Contents lists available at ScienceDirect

Results in Materials

journal homepage: www.sciencedirect.com/journal/results-in-materials

Corrosion and wear interplay: Tribo-electrochemical evaluation of NiTiNOL60 alloy in sulfuric acid

Anthony Onyebuchi Okoani [a,c,**], Ashveen Nand [b], Maziar Ramezani [a,*]

[a] Department of Mechanical Engineering, Auckland University of Technology, Auckland, New Zealand
[b] Faculty of Engineering, University of Auckland, Auckland, New Zealand
[c] Department of Mechanical Engineering, University of Nigeria, Nsukka, Nigeria

ARTICLE INFO

Keywords:
NiTiNOL60 alloy
H_2SO_4 electrolyte
Tribocorrosion
Wear mechanisms

ABSTRACT

The combined corrosion and wear behaviour of NiTiNOL60 alloy is important in various engineering applications. While previous studies have explored its performance in artificial seawater environments, limited information exists regarding its tribocorrosion characteristics in acidic conditions. This paper investigates the synergistic interaction between sliding wear and electrochemical processes for NiTiNOL60 alloy in a sulfuric acid environment, employing experimental procedures compliant with ASTM standards. Microscopic analysis confirms the alloy's Ni-rich composition, featuring a dense network of B2 NiTi + Ni_4Ti_3 cubic and rhombohedral crystal matrix structures. Our research and results reveal that material degradation during tribocorrosion arises from the combined effects of sliding wear and electrochemical reactions. Consequently, multiple wear mechanisms influenced by tribochemical wear are observed, with delamination and micro-cracks being notably prominent under higher applied loads due to surface tensile stress and contact pressure, leading to crack propagation perpendicular to the sliding direction. These findings have practical implications for optimising the performance and durability of NiTiNOL60 alloy in acidic environments, offering valuable insights for load-bearing engineering applications.

1. Introduction

Tribocorrosion, the synergistic interaction between mechanical wear and corrosion, is a critical concern in various applications, including engineering and biomedical, where metallic components are exposed to sliding or rolling contact in corrosive environments [1,2]. It is a significant concern in various industrial applications, such as automotive, spacecraft [3], marine [4,5], food and beverage processing [6–8], pharmaceutical [9], biomaterial [10,11], actuators [12] and biomedical sectors such as orthopaedic [13], endodontic [14] and orthodontic [11, 14]. According to Salas et al. [15], Ti–6Al–4V alloy (Ti64) gained vast application in the biomedical industry due to its outstanding corrosion resistance and good mechanical qualities. However, the toxicity of V (Vanadium) and Alzheimer's disease linked to Al have prompted researchers in the past decades to focus on developing new metallic materials free of harmful components [15]. In this regard, novel Ti-based alloys that only contain highly biocompatible elements like Ni, Nb, Zr, and Sn have been discovered. These alloys exhibit excellent biocompatibility, low elastic modulus, high specific strength, and adequate corrosion resistance for vast biomedical and engineering applications [11]. Notwithstanding the excellent properties, metallic components experience surface deformations during sliding or rolling contact under corrosive environments [16]. Among the different corrosive environments, acidic conditions pose unique challenges due to their aggressive nature, leading to accelerated material deterioration [17–19]. Considering the engineering materials used in the aforementioned sectors, NiTi alloys have shown superior wear resistance compared to other conventional materials such as steels, Ni-based, and Co-based tribo-alloys [20]. Accordingly, Nickel-titanium (Ni–Ti) alloy, such as NiTiNOL60, has been weighed as a suitable replacement for conventional metals and, as a result, has received considerable scientific attention due to their biocompatibility, unique shape memory and mechanical properties [21]. NiTiNOL was discovered by William J. Buehler and colleagues in the late 1950s at the Naval Ordinance Laboratory, USA, while working on shielding materials [20,22,23]; hence, the combined name of alloy with the laboratory, Nickel–Titanium Naval

* Corresponding author.
** Corresponding author. Department of Mechanical Engineering, Auckland University of Technology, Auckland, New Zealand.
E-mail addresses: anthony.okoani@aut.ac.nz (A.O. Okoani), maziar.ramezani@aut.ac.nz (M. Ramezani).

https://doi.org/10.1016/j.rinma.2023.100523
Received 23 October 2023; Received in revised form 26 December 2023; Accepted 27 December 2023
Available online 28 December 2023

Ordinance Laboratory - NiTiNOL. NITINOL exhibits better recovery from significant amounts of strain and can replicate its original shape owing to the shape memory property. The superelastic property of NiTi-based alloys ensures substantial recoverable strain during deformation caused by stress-induced martensitic transformation. At relatively low temperatures and under external force, the initial parent phase (austenite) transforms into a martensite phase accompanied by macroscopic deformation. The austenite phase undergoes a significant deformation during loading and subsequently transforms into detwinned martensite [24]. Martensite and austenite undergo a reversal transition upon unloading with significant recoverable strain [25,26]. Understanding the impact of strain rate on the tensile characteristics of superelastic NiTi has been the focus of extensive research. According to Neupane and Farhat [20], the superelasticity of NiTi under tensile loading conditions has demonstrated that the tension at the austenite to martensite transition increases with increasing strain rate. These microstructural changes significantly affect the wear and deformation behaviours of superelastic NiTi. Miller et al. [27] reported that Ni-rich NiTi alloys had gained interest as prospective materials for specialised bearing and gear applications in the last decade. Another study presented that NiTi alloy with a near-equal atomic ratio is often used in many applications, such as bearings and engine blocks, aerospace, communication, naval ships and medical devices due to its good shape memory effect or super-elasticity, high wear-resistant performance and superior corrosion resistance [28], yet NiTiNOL60 alloy may be subject to tribological conditions leading to wear [29].

When subjected to tribological conditions in acidic environments, the tribocorrosion behaviour of NiTi alloy becomes an essential consideration for its reliability and performance. Consequently, tribocorrosion has garnered significant research interest as scientists and engineers seek to unravel the underlying mechanisms and develop effective mitigation strategies. When contact bodies operate in a corrosive environment, surface chemical phenomena can significantly affect their deterioration. In this case, it is essential to ascertain the tribocorrosion behaviour of the material in a specific corrosive environment such as sulfuric acid. Thus, understanding the tribocorrosion behaviour of NiTiNOL60 alloy in acidic media is essential for optimising its performance and longevity. The aggressive nature of acidic environments can significantly influence NiTi alloys' degradation mechanisms, wear rates, and corrosion resistance. For example, under sliding or erosive conditions, the passive film can be removed by abrasion, thus exposing the underlying reactive material to more severe corrosion. On the other hand, surface films were found to modify the mechanical behaviour of the underlying metal and, thus, its wear response [30]. In another study, Muñoz and Espallargas [31] reported that mechanical parameters significantly affect the rate of electrochemical material removal, whereas the rate of mechanical material removal is dependent on the electrochemical conditions at the time. Furthermore, they defined the total wear volume (V_t), which is the sum of the material loss due to sliding wear (V_{mech}) and the material loss owing to corrosion or electrochemical oxidation (V_{chem}), as the mechanistic interpretation of the tribocorrosion phenomena. As reported, numerous variables, including load, sliding speed, surface films, temperature, hardness, and work-hardening, affect the contact surfaces in tribocorrosion. Hence, this present study aims to investigate the tribo-electrochemical behaviour of NiTiNOL60 alloy in a sulfuric acid (H_2SO_4) medium, with a focus on understanding the synergy between the specific wear rate and the associated tribo-electrochemical degradation mechanisms.

2. Experimental methods

2.1. Preparation of samples

The NiTiNOL60 samples were received from the National Aeronautics and Space Administration (NASA), Glenn Research Centre, Cleveland, Ohio. According to Stanford [32], the samples were prepared through the Hot Isostatic Pressing (HIP) method; the fabrication details are described in NASA's technical report [32,33]. The sample plates with dimensions 20 × 10 × 10 mm were ground and polished to a mirror-finish surface using grinder-polisher machines to obtain an oxide-free surface for the surface characterisations. Using Buehler Eco-Met 30, the samples were abraded on sandpapers of #180, 500, 1200, and 2400 grits having the corresponding grain sizes of 104, 35, 15, and 8 μm, respectively. Further, the abraded samples were polished mechanically on polishing surfaces (6 μm and 1 μm) and diamond pastes (6 μm and 1 μm) using a Struers LaboPol-2 machine. Subsequently, the mirror finish surfaces were cleaned ultrasonically in distilled water and absolute ethanol for 3 min, dried and then stored in an airtight container for further processing. The electrolyte used for this study was prepared using the standard operating procedure for preparing analytical reagents.

2.2. Sample characterisation

The polished surfaces were characterised at different magnifications using an optical microscope AMScope – Olympus BX51 and a Hitachi SU-70 scanning electron microscopy (SEM) coupled with energy dispersive x-ray spectroscopy (EDS) to ascertain the microstructural arrangements, elemental composition, and distribution at different phases. The surface roughness was examined using a Talysurf 50 Taylor Hobson stylus profilometer. While the sample's macro- and micro-indentation hardness were measured using Leco microhardness LM–800AT and a Rockwell hardness tester HR–150A, respectively. In order to conduct the microhardness tests, the specimen was clamped, focussed, and tested with 1.0 kgf throughout the course of a 10-s dwell period. The hardness was then determined by measuring the geometric characteristics of the indentation, such as the depth or surface area of the diamond-shaped impression on the surface under examination. With regard to the macro-indentation hardness test, a combination of major and minor loads of 150 (140 + 10) kg were loaded and unloaded, and the resulting values were recorded.

2.3. Tribo-electrochemical measurements

The polished sample was further prepared for electrochemical measurements since the specimen serves as the working electrode (WE). Therefore, a cable-banana plug terminal was fitted for the potentiostat connection, and to guarantee that all sample surfaces aside from the top surface, which had a 2 cm^2 exposed area, were coated, a non-conductive copper tape and plasti-Dip coating were used for isolation of the surfaces. The layer/coating allows interference-free electrochemical measurements while shielding the underlying metal from corrosive conditions. For the tribocorrosion measurements, we adapted various standards from the American Society for Testing and Materials (ASTM) for investigating the synergy between wear and corrosion [34], the standard test method for linear reciprocating ball-on-flat sliding [35], and the standard practice for electrochemical measurements in corrosion testing [36,37]. The experimental setup shown in Fig. 1 presents the coupling of a linear reciprocating ball-on-plate tribometer (DUCOM TR-282) and an electrochemical potentiostat cell (IviumStat) of three electrode configurations. The test parameters for electrochemical measurements call for stabilisation at the open circuit potential (OCP) for 1200 s, a scan rate of 2 mV/s, an applied voltage range of −5.0 V to +7.0 V for potentiodynamic measurements within a 100 mV potential step for about 60 min, and a re-conditioning time of 20 min. While the test conditions for a reciprocating sliding wear test conducted at a room temperature of ~22 °C include a sliding frequency of 4 Hz, applied normal loads of 2, 5 and 8 N, a stroke length of 10 mm, and a sliding duration of 6250 s for a tribo-corrosion test.

As shown in Fig. 1, the electrodes, including the calomel reference electrode (RE) filled with 3 M KCl, the graphite rod counter electrode (CE) as well as the specimen (WE) clamped onto the tribometer test cell

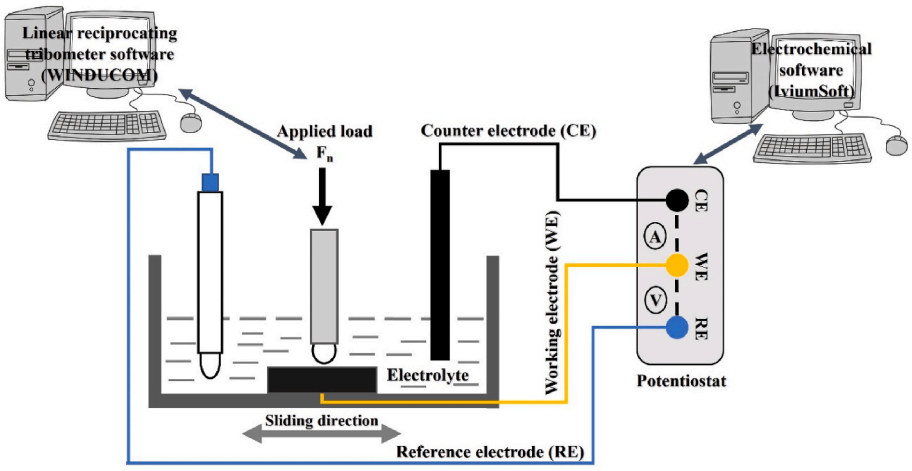

Fig. 1. Experimental setup for tribocorrosion of NiTiNOL60 alloy in H_2SO_4 solution.

holder and fully immersed in H_2SO_4 electrolyte were connected to the potentiostat. The series connection between CE and WE aimed to measure the corrosion current (A) between the anode and cathode terminals, while the WE and RE linking measures the sample's potential (V). The normal load was applied to the WE, coupled to the mounted counter body (alumina ball – Al_2O_3) of Ø 10 mm. The system was allowed to reach a steady state in open circuit potential (OCP) mode prior to the tribocorosion measurements, which were then performed simultaneously with potentiodynamic polarisation measurements and the reciprocating sliding of an Al_2O_3 ball against the contact surface NiTiNOL60 sample. During the measurements, the sliding wear signals, such as the frictional forces and the electrochemical parameters, were transmitted and registered on the data acquisition tools: WINDUCOM software and IviumSoft, respectively. For accuracy and repeatability, each test was repeated three times with a fresh surface of Al_2O_3 revealed each time to slide against the stationary NiTiNOL60 sample in the corrosive medium. After each test, the sample was cleaned ultrasonically with absolute ethanol and dried for further surface examinations on the wear track created during sliding to reveal the wear mechanisms, re-measure surface roughness and hardness and quantify the material loss due to the wear and corrosion synergistic interactions.

2.4. Wear measurements and re-characterisations of the surfaces

In order to understand the wear rate at different conditions following the wear scar created at the contact surfaces, measuring the material losses (wear volume) and specific wear rates is essential. Hence, the surface roughness of the wear tracks at different applied loads was measured using a Taylor Hobson Form Talysurf 50 stylus profilometer for this measurement. About five parts of the wear tracks were inspected for the wear volume measurements, with the stylus tip positioned to move vertically along the wear track. This produced a two-dimensional surface height and distance output along the measured lines. The output data was a raw profile chart displaying the sample's worn surface's roughness, waviness, asperities, grooves, etc. We used ImageJ, a software program for image analysis, to quantify the wear scars' size because the graphical representation profiles made it possible to measure their depth and width. The wear track's area was then determined using the estimated parameters, and this aided the calculation of the volume loss by multiplying the area by the reciprocating stroke length, which is 10 mm. Equation (1), derived from Archard's wear law expression, computed the specific wear. According to the expression, wear rate quantifies the material yielding under specific operating conditions per unit time [19].

$$\text{Specific wear rate, } \dot{W}\ (\text{mm}^3/\text{Nm}) = \frac{\text{Wear volume}}{\text{Normal load x Sliding distance}} \quad (1)$$

The Butler-Volmer expression, combining Tafel equations for the cathodic and anodic regions, is used to calculate the electrochemical parameters. The expression shown in Equation (2) calculates the corrosion rate [38].

$$\text{Corrosion rate, C.R (mmpy)} = \frac{0.13A * i_{corr} * M}{n * \rho} \quad (2)$$

where i_{corr} = corrosion current density (A/cm^2), A = area (cm^2), M = atomic mass of the metal (g/mol), n = number of electrons/atoms produced or consumed in the redox reaction while ρ = density of the material (g/cm^3), and 0.13 = time conversion factor per unit area of the exposed surface. This investigation employed the IviumSoft tool for corrosion analysis using the electrochemical parameters registered during tribocorrosion.

3. Results and discussion

3.1. Surface characterisation

The metallographic investigation was conducted using the optical microscope, SEM and EDS. Fig. 2 shows the SEM-EDS and the quantitative composition analysis of the NiTiNOL60 sample. For the SEM, a 20 KV penetrating voltage was used to scan the sample surface at full scale to ensure adequate penetration of the X-rays through the subsurface regions. Using EDS to quantify the elemental compositions and characterise the polished sample, the spectral image and the accompanying table present the quantitative compositions of the material investigated. The analysis confirmed that the specimen was a binary nickel-titanium alloy containing 60 wt% Ni and 40 wt% Ti (55 at.% Ni, 45 at.% Ti), i.e., a Ni-rich intermetallic NiTiNOL60 alloy [27,39]. This was in good agreement with the compositions of NiTiNOL60 alloy previously reported in the literature [27].

To examine the subsurface of the sample on a microscopic scale, the cross-sectional part of the sample was obtained through wire cutting, abraded, polished, and etched using Kroll's reagent: 82.7 % H_2O, 14.1 % HNO_3, and 3.2 % HF for 30 s. This revealed the microstructural compositions of the sample presented in the microscopic image in Fig. 3. The examination under the optical microscope reveals the microstructural arrangement of NiTiNOL60 alloy with distinct regions of consolidated and unconsolidated grain network clusters. The majority of the micrograph image is represented by the NiTi + Ni_4Ti_3 region composed of ordered cubic and rhombohedral crystal matrix structures [25,40] and

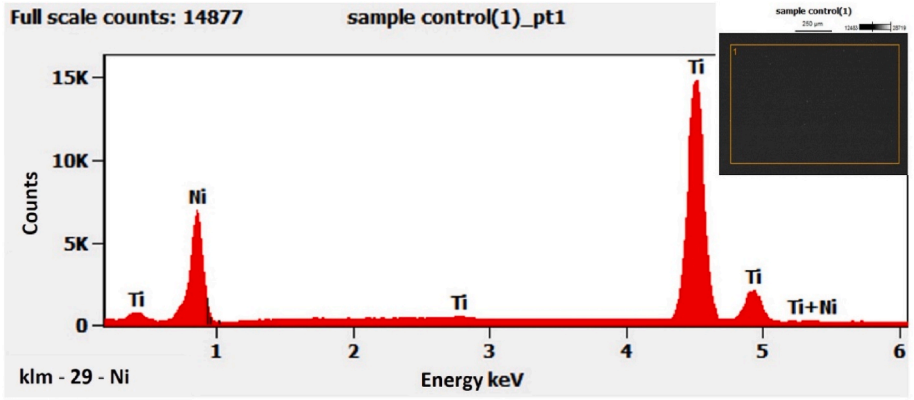

Weight %

	Ti	Ni
sample control(1)_pt1	40.14	59.86

Fig. 2. EDS spectral imaging of the polished NiTiNOL60.

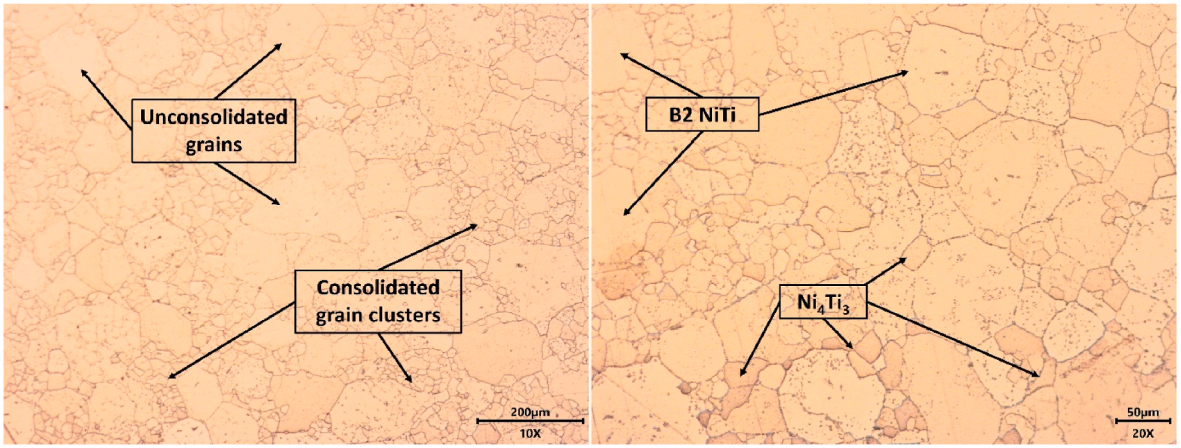

Fig. 3. Optical microscopic images of NiTiNOL60 at different magnifications.

fine and coarse grain network structures [41]. The dense network of unconsolidated and consolidated grain clusters reveals the inhomogeneity in the microstructural grains [39,42], thus supporting the non-equi-atomic elemental distribution shown in Fig. 2, which tends to have Ni-rich or Ti-rich zones [43]. The dominance of the B2 NiTi and Ni_4Ti_3 matrix highlighted in the micrograph suggests globular and needle-like shaped precipitates B19′ in the B2 matrix [21,23].

3.2. Frictional behaviour during reciprocating sliding

During the reciprocating sliding wear tests, the frictional behaviours were monitored, and the measured parameters were recorded on the WINDUCOM software tool. The parameters were analysed to determine the material's coefficient of friction (CoF) characteristics over the course of the reciprocating sliding. As shown in Fig. 4, the CoF is plotted as a function of sliding time for three applied loads. Clearly, at the initial sliding stage, the applied load had a reasonable running-in time characterised by the interfacial friction interactions leading to the breakdown of oxide layers [44,45], localised heating of the contact surfaces and oxidation of asperities. The fluctuations recorded in the CoF plots could be attributed to the distortions caused by wear debris and formed layers (passivation) during tribocorrosion. Based on the CoF plots, the applied load of 2 N required a longer running-in time to wear the passive layer, unlike the 5 N and 8 N loads. At higher loads (5 N and 8 N), it is evident that the contact surfaces overcame a running-in time during the

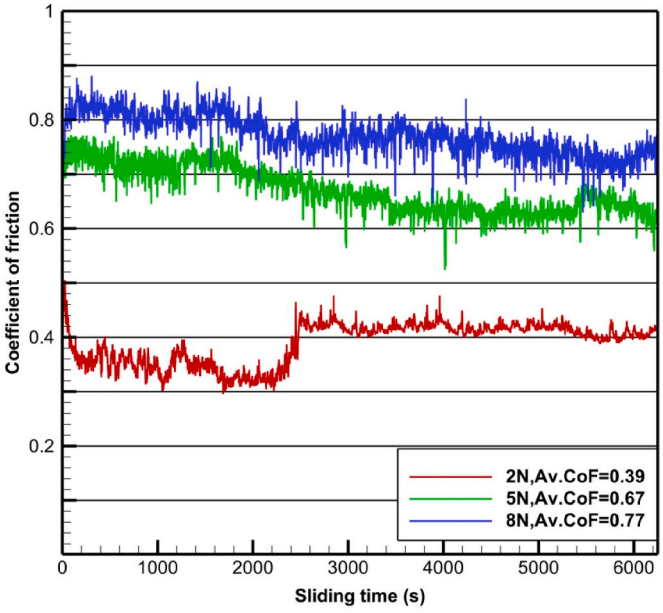

Fig. 4. Friction coefficient plot against sliding time.

continuous sliding by removing the passive layer, penetrating and wearing off the sample surface, and eventually exposing the material sub-surface. Whereas, for an applied load of 2 N, the CoF increased after 30 min of break-in point, whereby the passive film on the sample surface was destroyed and maintained approximately 0.4 CoF throughout the sliding duration until a steady-state value was attained. As the contact pressure increases, the passive layers are easily destroyed through a continuous reciprocating sliding contact; this creates more surface roughness and widens the wear track, thereby increasing the surface area available for oxidation. The examined surfaces in Fig. 5 micrographs show the least amount of chemical and mechanical wear mechanisms for the 2 N load when compared with the other loads investigated. According to Zeng and Dong [46], friction is most severe at higher loads, and this is supported by the results obtained for the 8 N load with the highest average CoF $\mu = 0.77$, maximum wear volume alongside the increased chemical and mechanical mechanisms.

3.3. Surface examination

The sliding actions of the contact surfaces created a wear track within the sliding stroke length of 10 mm. Examining the wear scar reveals mild to severe wear mechanisms, with delamination and adhesive wear being more predominant. The recorded wear mechanisms conform with the four main mechanisms of adhesive wear, abrasive wear, fatigue wear and tribochemical wear reported in the literature [31,47]. Following the SEM images in Fig. 5, the specimen investigated at 2 N, 4Hz condition shows little detachment and adhesion of the wear debris. In contrast, the SEM micrographs at higher loads show extensive abrasion and delamination, which propagates when subjected to various loading conditions. The rate of abrasion and depassivation could be attributed to a number of variables, including the mechanical characteristics of the metal, the contact geometry, the applied force, and the effects of hydrodynamic lubrication [48]. From the results, micro-cracks were discovered to be more pronounced at 8 N load, and it is believed to have developed from surface tensile stress and extended perpendicular to the direction of sliding. While corrosion pits progressed from the initial nucleation stage into metastable pit formation and stable pitting [49]. Our analysis shows that corrosion pit nucleation and micro-crack propagation were promoted by the contact pressure on the interacting surfaces and the third-body wear effects [50].

Considering the high level of adhesion, it was imperative to further examine the wear tracks using the EDS characterisation technique to determine the makeup of the surface wear particles. Fig. 6 presents the EDS results, which revealed oxidation and Al debris as the elemental compositions detected along the wear tracks. The overall scan of the surfaces represented by point 1 shows that the oxide composition increases with load increase while the adhesion of the Al debris decreases. The increased oxidation promoted electrochemical activities and subsequently resulted in increased corrosion rate.

Since Al debris formed the greater composition of elements detected along the wear track of NiTiNOL samples, there was a need also to investigate the sliding surfaces of the counter material (Al_2O_3 ball) sliding against NiTiNOL60 alloy. From Fig. 7, it can be established that the rate of material detachment and adhesion onto the contact surfaces occur simultaneously. As shown in the image, the ball surface revealed wear debris, and further examination of the surfaces at different applied loads presents the spectral images as well as their corresponding elemental compositions. The surfaces were clearly oxidised in the electrolyte mediums, and the oxide contents decreased with increasing load. Conversely, the deposition of the Ni–Ti wear debris increased as the contact pressure increased, thereby breaking down the oxidised layer and enhancing the material detachment and adhesion. As the contact pressure at 2 N was not adequate to break in the material surface, this shows why the greater surface was oxidised, whereas the continuous reciprocating sliding at higher loads caused the breakdown of the oxide layers. Points 2 reveal Ni and Ti as the adhered material onto the ball surface, while point 3 confirms the alumina as the base material, with Al having the maximum percentage composition. In light of this, it is evident that the significant impact of contact pressures at higher applied loads leads to the detachment of the interacting surfaces asperities, which then initiates abrasion and adhesion mechanisms.

The EDS results in Fig. 7 were further examined using the spectral imaging technique to analyse the alumina ball sliding surface at 8 N load. The spectral imaging depicted in Fig. 8 clearly identifies the oxidised points on the surfaces as the bright patches shown in the purple tint. The yellow colour distribution across the micrograph determines the base material (alumina ball) with black patches of the wear debris adhesion. While the blue and red colours highlight the Ti and Ni wear debris adhesion, which is attached to the ball surfaces during sliding contact.

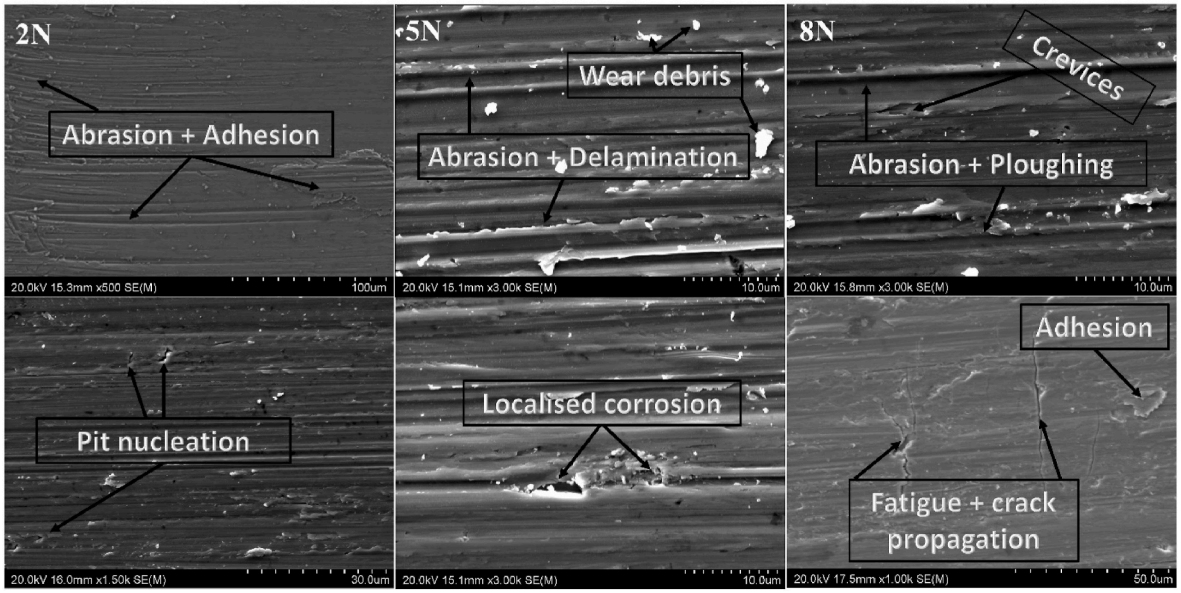

Fig. 5. SEM examination revealing the wear mechanisms during tribocorrosion.

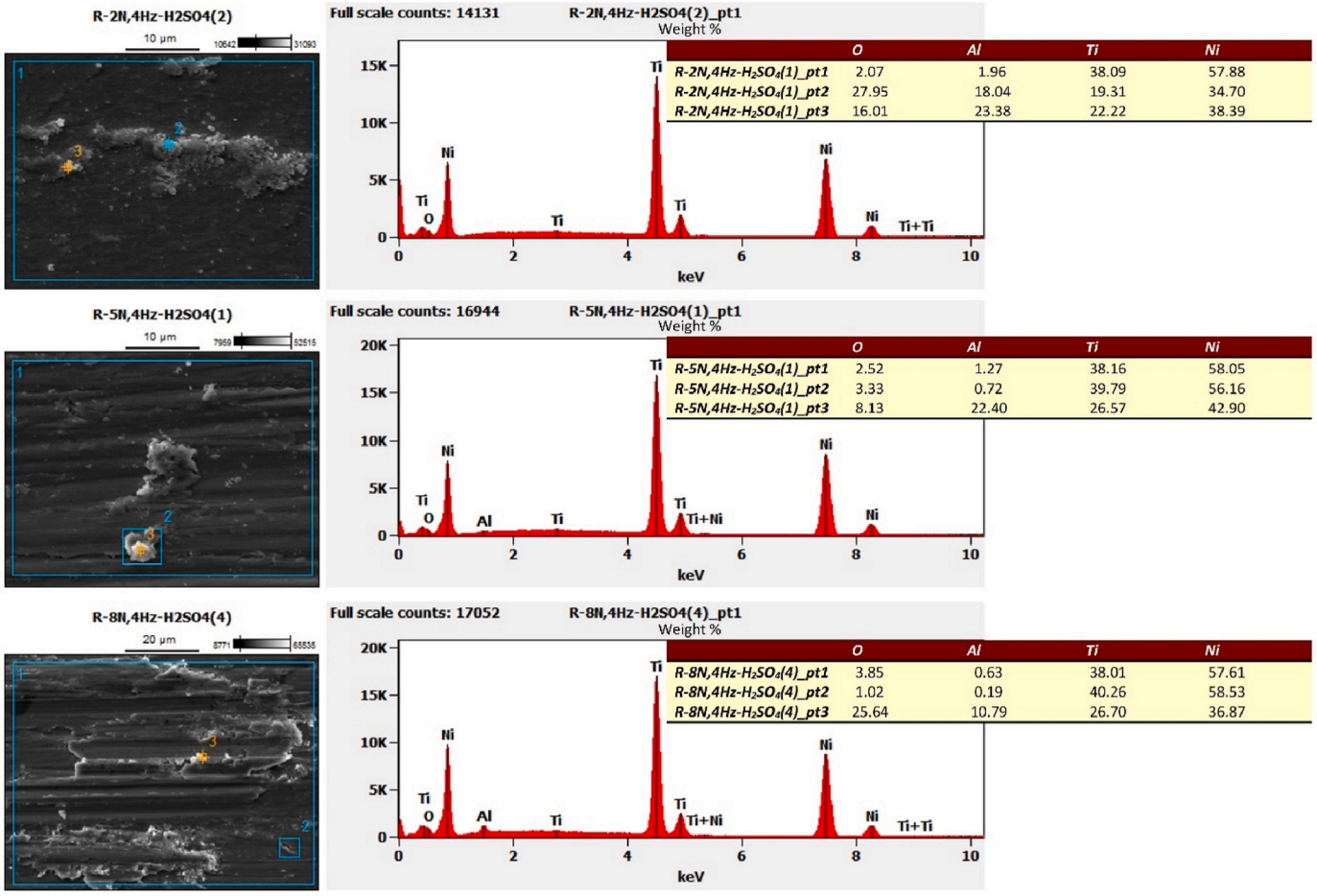

Fig. 6. EDS examination of wear debris adhesion along the sample wear track.

3.4. Potentiodynamic polarisation

The potentiodynamic polarisation was used to investigate the passivation behaviour of the NiTiNOL60 alloy under tribocorrosion conditions in an acidic solution, and the results are presented in Table 1 and Fig. 9. From the Tafel plots, it is evident that the anodic domain of the polarisation curve is initiated with an active dissolution region, where metals are easily converted to ions and transported to electrolyte solutions and eventually enter a passive region following passivation [11,51]. According to Ghali [49], the electrochemical breakdown of oxides of some metals is reduced cathodically to the metals or ions in aqueous solutions. The curves clearly show that corrosion occurred in the cathodic and anodic regimes with distinctive passivation regimes. The specimens investigated at 5 N and 8 N loading conditions exhibited similar passivation behaviours, while the E_{corr} values became more positive as the load increased. This deduction aligns with the findings presented by Salas et al. [15].

Analysis of the Tafel plots gave rise to the following parameters presented in Table 1. The table denotes the electrochemical activity of the material during tribocorrosion as well as the fitted parameters. Tafel analysis provided information on variables like corrosion potential, corrosion current density, passivation resistance, as well as corrosion rate; whereas the model data presents a good fit. According to our analysis, an increase in the applied load increased the corrosion current while the corrosion potential tends towards zero; this caused the polarisation resistance to continuously decrease and, in turn, increased the corrosion rate. The increase in i_{corr} values is correlated with the progression of the sample's corrosion rate (Cr); this is inversely connected to their polarisation resistance (Rp) values [15]. This demonstrates that the corrosion potential, which controls the anodic or cathodic polarisation activity, governs the dissolution rate of metals [19,52].

Considering the wear mechanisms shown in Fig. 5 and the corrosion effect, an etched cross-section of the sample was examined to ascertain the propagation of corrosion pits and cracks beyond the contact surface. Fig. 10 presents the SEM micrograph, EDS spectrum and the corresponding elemental distributions as shown in the table. The results show localised corrosion, such as pit and crevice, occurred during tribocorrosion. The corrosion pit and cavities shown could be attributed to the corrosion-abrasion synergy, which impedes the reactivity between the anode surface and the electrolyte [53,54]. Further examination of the pit using EDS reveals the maximum oxygen concentration for points 1 and 2 at the pit region. At point 3, a decline in the oxide composition was recorded, showing that oxidation promoted the pit nucleation. Point 4 confirms the exact composition of the material with no oxygen concentration.

3.5. Hardness measurement

To ascertain the effect of tribocorrosion on the specimen, micro- and macro-indentation hardness measurements were carried out using the methods outlined in sub-section 2.2. Prior to the tribocorrosion testing, the sample's average Rockwell hardness of the specimen was measured, and it was found to be 62.5 HRC, which is consistent with the values reported in the literature [22,55,56]. Measurements after the testing reveal that the sample's average macro hardness, as determined by the Rockwell Hardness test, was 63.3 HRC. Whereas the micro-indentation Vicker's hardness along the wear track presents the average values of

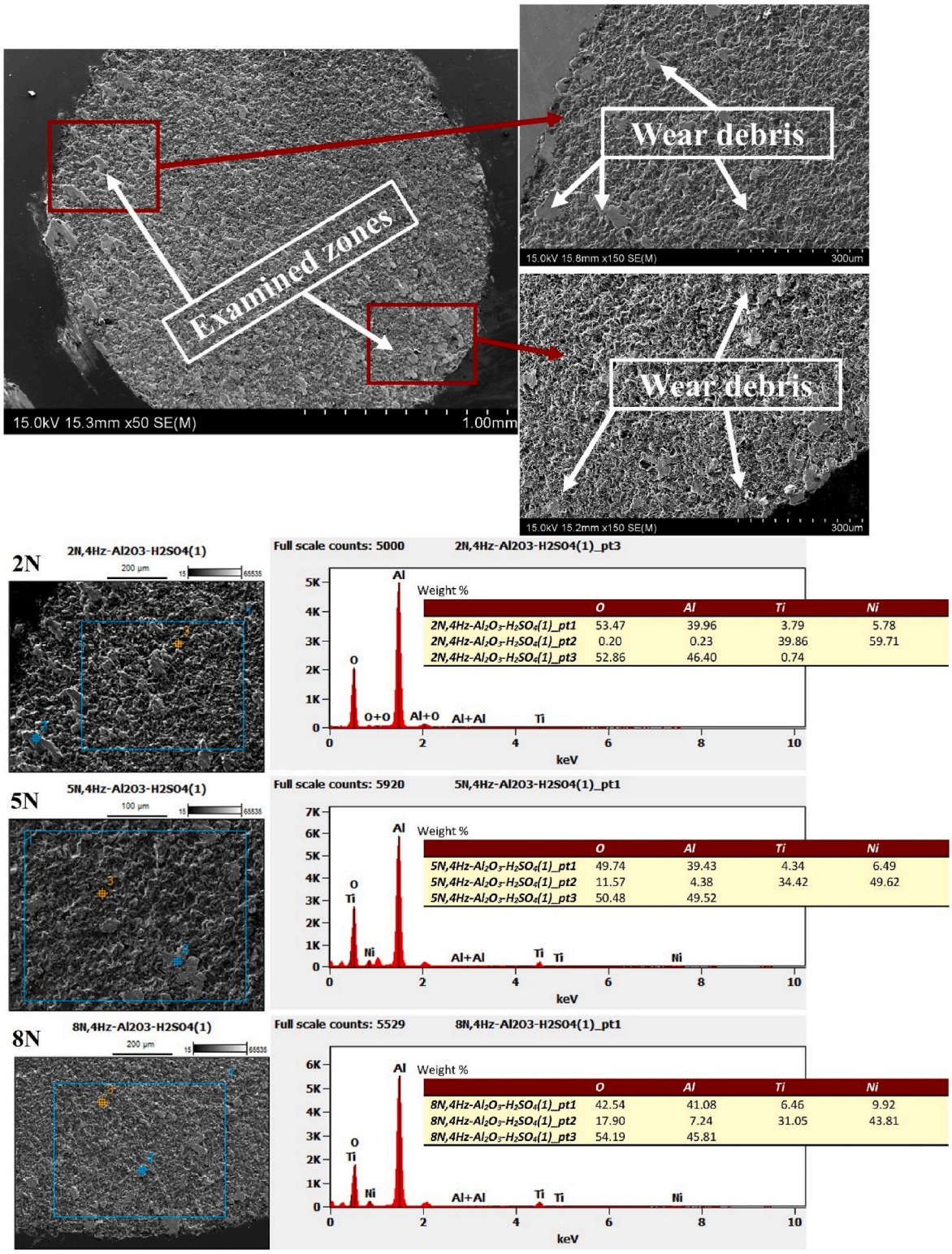

Fig. 7. SEM and EDS characterisation of the counter material (Al_2O_3 ball) sliding surface.

Hv (537.93/1.0kgf/10s, 547.77/1.0kgf/10s and 578.83/1.0kgf/10s) for 2 N, 5 N and 8 N respectively. In contrast, the measurement outside the wear track had a relatively lower Vicker's hardness value of HV 537.83/1.0kgf/10s. As the applied load increased, the hardness values along the wear track increased, and the recorded high values could be attributed to work-hardening as a result of compressive forces and precipitation hardening through the rapid formation of nanoscale Ni_4Ti_3 precipitates during sliding [27,57,58]. Also, the non-uniform network structures in Fig. 3 could contribute to the variations in the micro-hardness values along the wear track [41].

3.6. Contact surface interactions and tribo-corrosion mechanisms

During tribocorrosion, the simultaneous actions promoted an

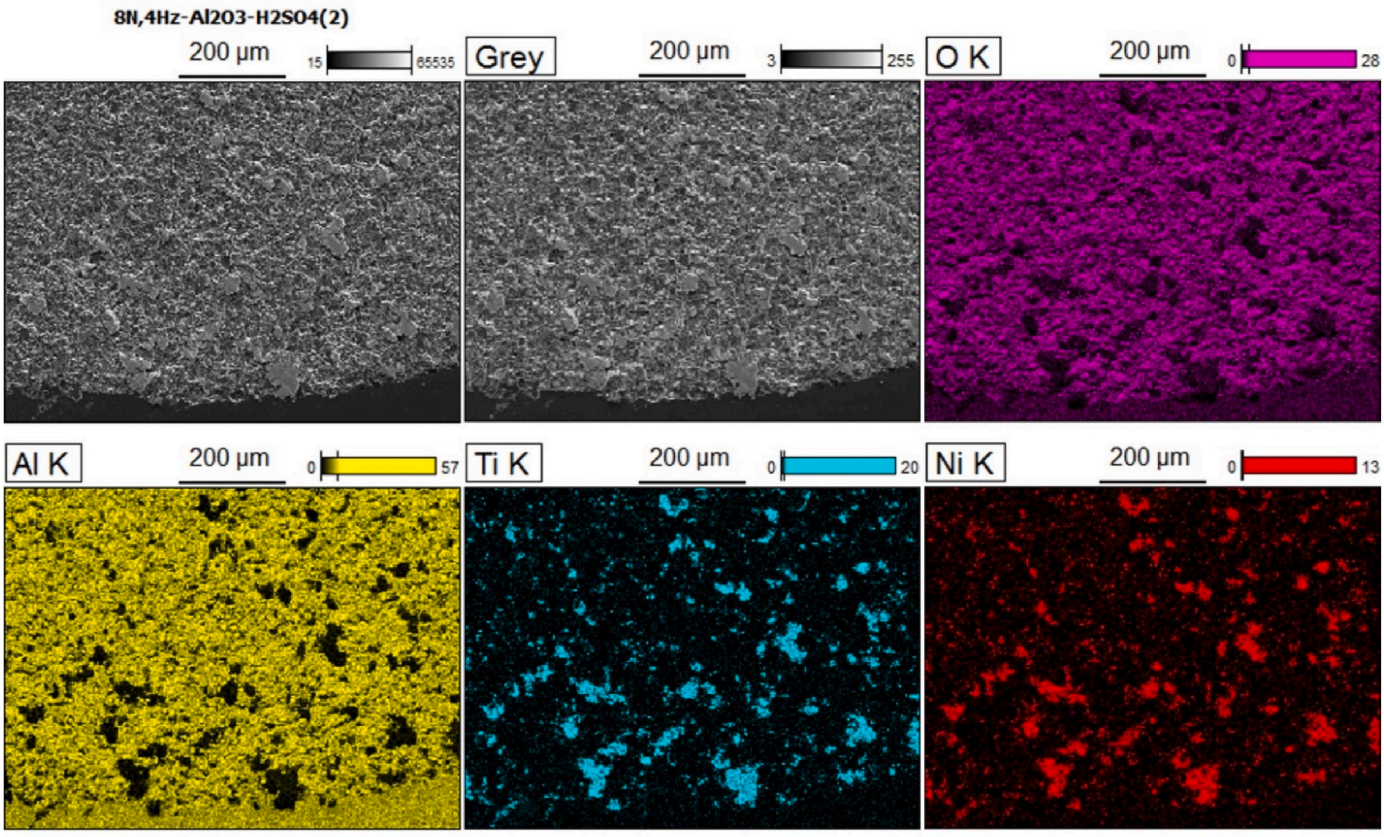

Fig. 8. EDS spectral imaging of the counter material (Al_2O_3 ball) surface at 8 N applied load.

Table 1
Electrochemical parameters from corrosion rate analysis following the potentiodynamic polarisation measurements.

Corrosion rate analysis	Pol. Res. 2 N 5 N 8 N			Tafel data 2 N 5 N 8 N			Model data 2 N 5 N 8 N		
E_{corr} (V)	−0.167	−0.322	−0.506	−1.842	−1.257	−1.171	−0.226	−0.507	−0.699
$I_{corr.}$ (A)	2.988E-5	3.424E-5	4.182E-5	1.451E-3	1.795E-3	2.565E-3	1.181E-3	1.148E-3	1.425E-3
$_{Icorr.}$ (A/cm^2)	7.312E-7	8.378E-7	1.023E-6	3.55E-5	4.392E-5	6.276E-5	2.889E-5	2.808E-5	3.487E-5
R_p (ohm)	726.700	634.100	519.200	743.400	436.900	295.400	616.300	397.400	309.600
ba V/dec	–	–	–	5.748	4.843	5.623	3.024	2.186	2.359
bc V/dec	–	–	–	4.372	2.878	2.530	3.756	2.021	1.784
C. Rate (mm/y)	0.023	0.027	0.033	1.143	1.411	2.017	0.928	0.902	1.120

increase in the oxidation of the exposed surfaces. While sliding contacts initiated the breakdown of the passive films, which led to delamination, mild to severe abrasion, and adhesion, the oxidised surfaces promoted localised corrosion, as demonstrated by the SEM and EDS characterisations [51]. Liu et al. [11] presented in their study that while surface defects promote passivation rates in the early stages of exposure, corrosion protection is best at a slowly formed passive film. It is established that the corrosion damage mechanism at the asperities of contact surfaces involves mechanical and chemical components, with the observable damage typically coming from both [31]. Hence, the synergistic interactions resulted in material losses and various wear mechanisms caused by the mechanistic approach, which involves the primary contributions of mechanical wear and wear-accelerated corrosion, i.e., anodic dissolution [59,60]. Considering the tribocorrosion synergistic interactions, the contributing mechanisms are investigated following the wear behaviours revealed in Fig. 5 and computing the specific wear rate using Equation (1). The results are shown in Fig. 11, which compares the specific wear rate and the polarisation resistance during electrochemical measurements. It is evident from the graphical trend that increased applied load reduces the polarisation resistance, which in turn amounts to an increased corrosion rate. This demonstrates that the material yield due to the synergy between wear and corrosion is larger than the effects of each factor acting alone [61]. The constant rubbing of the contact surfaces during reciprocating sliding results in the wear mechanisms caused by the high level of material detachment following the synergistic interplay between mechanical and electrochemical processes [62].

4. Conclusion

The present study investigated the simultaneous interactions of wear and corrosion in a dilute sulfuric acid solution under varied applied loads. The experimental results provided insights into the tribocorrosion behaviour of NiTiNOL60 alloy in an acidic environment. The results show that material losses under tribocorrosion conditions are significantly influenced by the synergistic interaction between wear and corrosion. SEM/EDS metallographic investigation depicts that B2 NiTi and the stable Ni_4Ti_3 matrix structures dominate the NiTiNOL60 alloy microstructural network. As shown from our analyses, the mechanical action frequently results in the local removal of metal and oxide

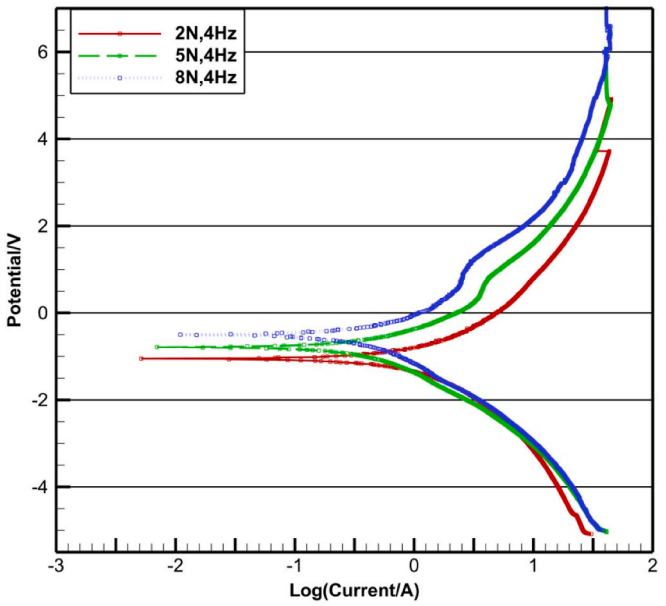

Fig. 9. Tafel plots at different applied loads after potentiodynamic polarisation measurements using a Calomel reference electrode.

particles, thereby exposing the metal surface, which is subsequently followed by a repassivation process. The main mechanism under sliding investigation is abrasive wear, whereas oxidative wear predominates in the electrochemical regime, triggering a cathodic shift during potentiodynamic polarisation measurements. Additionally, the degree of this shift increases with the increase of applied normal load due to depassivation under sliding contact. It is established that the delamination and, subsequently, plastic deformation of the material surface during depassivation were influenced by the initiation and propagation of pits and micro cracks on the passive layer during repeated sliding. Thus, the contact pressure on the interacting surfaces promoted

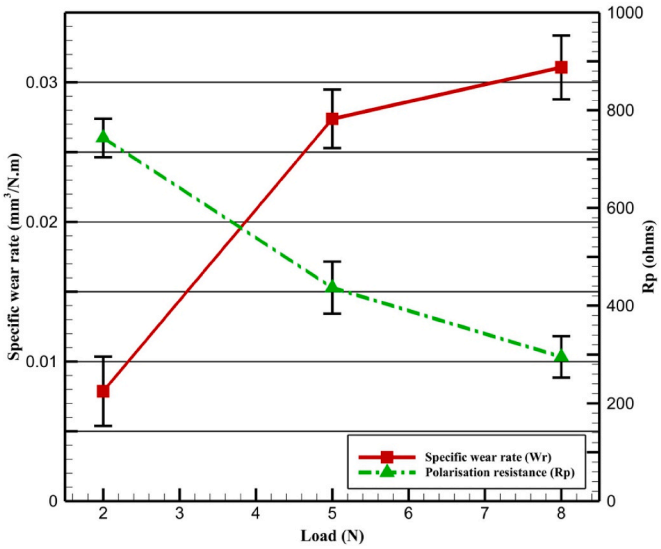

Fig. 11. Specific wear rate and polarisation resistance relationship.

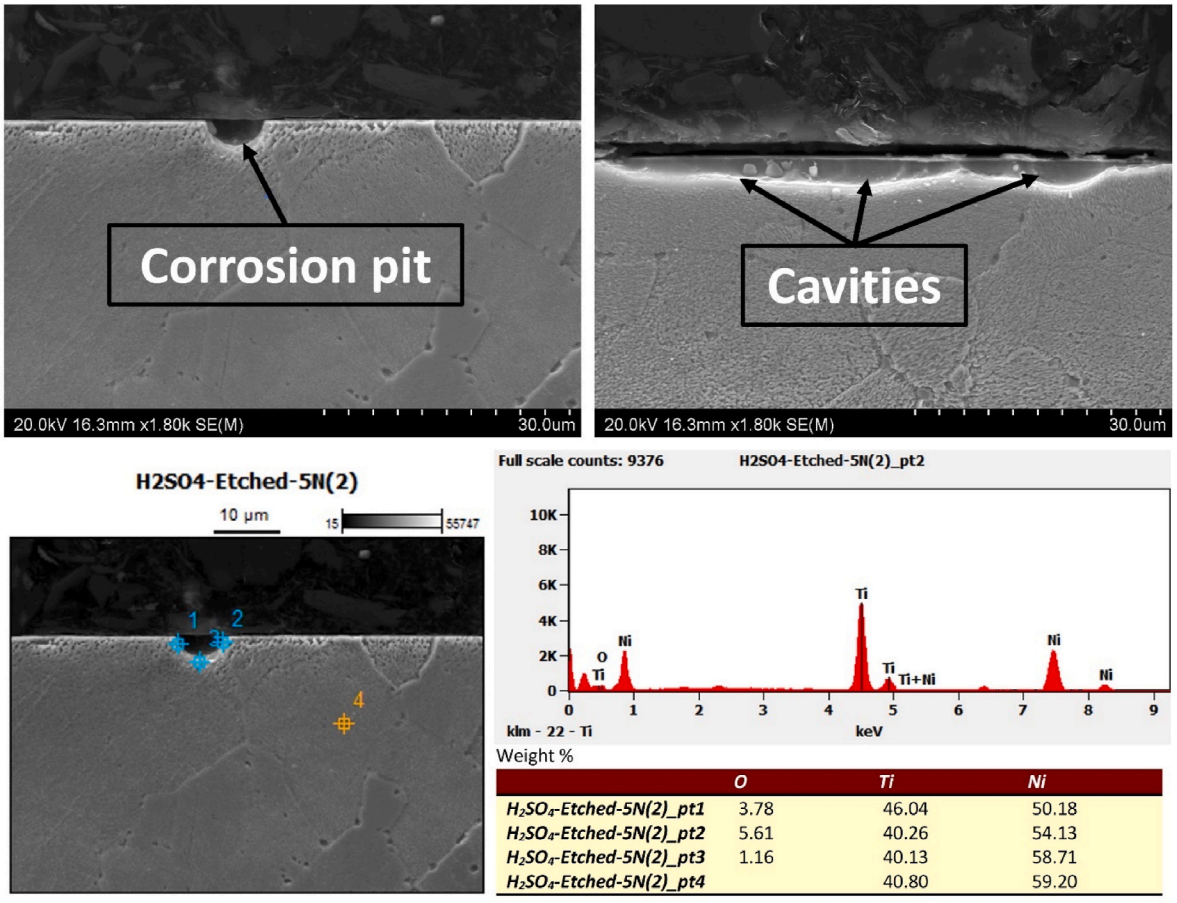

	O	Ti	Ni
H_2SO_4-Etched-5N(2)_pt1	3.78	46.04	50.18
H_2SO_4-Etched-5N(2)_pt2	5.61	40.26	54.13
H_2SO_4-Etched-5N(2)_pt3	1.16	40.13	58.71
H_2SO_4-Etched-5N(2)_pt4		40.80	59.20

Fig. 10. SEM-EDS characterisation of localised corrosion on the material subsurface.

corrosion pit nucleation and micro-crack propagation.

CRediT authorship contribution statement

Anthony Onyebuchi Okoani: Conceptualization, Data curation, Formal analysis, Investigation, Methodology, Writing - original draft, Writing - review & editing. **Ashveen Nand:** Methodology, Supervision, Writing - review & editing. **Maziar Ramezani:** Conceptualization, Funding acquisition, Methodology, Project administration, Resources, Supervision, Writing - review & editing.

Declaration of competing interest

The authors declare that they have no known competing financial interests or personal relationships that could have appeared to influence the work reported in this paper.

Data availability

Data will be made available on request.

Acknowledgment

The authors express their gratitude to Dr. Christopher DellaCorte for providing the NiTiNOL60 samples used in this study for testing and analysis.

References

[1] A.I. Munoz, N. Espallargas, S. Mischler, Tribocorrosion phenomena and concepts, in: A. Tribocorrosion, N. Espallargas Igual Munoz, S. Mischler (Eds.), Switzerland: Springer Briefs in Applied Sciences and Technology, Springer, Cham, 2020, pp. 35–42, ch. 4.
[2] S. Mischler, A.I. Munoz, Tribocorrosion, in: K. Wandelt (Ed.), Encyclopedia of Interfacial Chemistry, Elsevier, Oxford, 2018, pp. 504–514.
[3] S.V. Pepper, C. DellaCorte, R.D. Noebe, D.R. Hull, G. Glennon, Nitinol 60 as a material for spacecraft triboelements, in: Presented at the 13th European Space Mechanisms and Tribology Symposium - ESMATS 13 Conference, Vienna, Austria, September 22-27, 2009. Conference Paper. [Online]. Available: https://ntrs.nasa.gov/api/citations/20090034488/downloads/20090034488.pdf.
[4] R.J.K. Wood, Marine wear and tribocorrosion, Wear 376–377 (2017) 893–910, https://doi.org/10.1016/j.wear.2017.01.076.
[5] R. Johnsen, C.B. Von Der Ohe, 16 - tribocorrosion in marine environments, in: D. Landolt, S. Mischler (Eds.), Tribocorrosion of Passive Metals and Coatings, Woodhead Publishing, 2011, pp. 441–474, ch. 16.
[6] M. Atapour, I. Odnevall Wallinder, Y.S. Hedberg, Stainless steel in simulated milk and whey protein solutions - influence of grade on corrosion and metal release, Electrochim. Acta 331 (2020), https://doi.org/10.1016/j.electacta.2019.135428. Art no. 135428.
[7] S. Varmaziar, M. Atapour, Y.S. Hedberg, Corrosion and metal release characterization of stainless steel 316L weld zones in whey protein solution, npj Mater. Degrad. 6 (2022) 1–9, https://doi.org/10.1038/s41529-022-00231-7.
[8] M.S. Jellesen, M.Ø. Hansen, L.R. Hilbert, P. Møller, Corrosion and wear properties of materials used for minced meat production, J. Food Process. Eng. 32 (4) (2009) 463–477, https://doi.org/10.1111/j.1745-4530.2007.00223.x.
[9] A. Zaffora, F.D. Franco, M. Santamaría, Corrosion of stainless steel in food and pharmaceutical industry, Curr. Opin. Electrochem. 29 (2021) 1–7, https://doi.org/10.1016/J.COELEC.2021.100760. Art no. 100760.
[10] A. Wadood, Brief overview on NiTinol as biomaterial, Adv. Mater. Sci. Eng. (2016) 1–9, https://doi.org/10.1155/2016/4173138, 2016.
[11] M. Liu, J.-N. Zhu, V.A. Popovich, E. Borisov, J.M.C. Mol, Y. Gonzalez-Garcia, Corrosion and passive film characteristics of 3D-printed NiTi shape memory alloys in artificial saliva, Rare Met. 42 (9) (2023) 3114–3129, https://doi.org/10.1007/s12598-023-02329-6.
[12] L.A. Khan, E. McCarthy, C. Muilwijk, I.U. Ahad, D. Brabazon, Analysis of nitinol actuator response under controlled conductive heating regimes, Results in Engineering 18 (2023/06/01/2023) 1–11, https://doi.org/10.1016/j.rineng.2023.101047. Art no. 101047.
[13] Y. Xue, Y. Hu, Z. Wang, Tribocorrosion behavior of NiTi alloy as orthopedic implants in Ringer's simulated body fluid, Biomedical Physics and Engineering Express 5 (4) (2019) 1–9, https://doi.org/10.1088/2057-1976/ab1db0. Art no.
[14] L.A. Dobrzański, L.B. Dobrzański, A.D. Dobrzańska-Danikiewicz, J. Dobrzańska, Nitinol type alloys general characteristics and applications in endodontics, Processes 10 (2022) 1–59, https://doi.org/10.3390/pr10010101. Art no. 101.
[15] L. Salas, et al., Tribocorrosion and corrosion behavior of quaternary Ti-24Nb-xZr-ySn alloys in SBF, Mater. Lett. 283 (2021), https://doi.org/10.1016/j.matlet.2020.128903. Art no. 128903.
[16] J. Zupanc, N. Vahdat-Pajouh, E. Schäfer, New thermomechanically treated NiTi alloys – a review, Int. Endod. J., Review 51 (10) (2018) 1088–1103, https://doi.org/10.1111/iej.12924.
[17] A. Dalmau, C. Richard, A. Igual – Muñoz, Degradation mechanisms in martensitic stainless steels: wear, corrosion and tribocorrosion appraisal, Tribol. Int. 121 (2018) 167–179, https://doi.org/10.1016/j.triboint.2018.01.036.
[18] S. Cao, S. Mischler, Tribocorrosion of a CoCrMo alloy in sulfuric acid – Glycerol mixtures, Wear 458–459 (2020), https://doi.org/10.1016/j.wear.2020.203443. Art no. 203443.
[19] A. Okoani, A. Nand, M. Ramezani, Tribocorrosion behaviour of NiTiNOL60 alloy in an alkaline environment, Results in Engineering 19 (2023) 1–11, https://doi.org/10.1016/j.rineng.2023.101305. Art no. 101305.
[20] R. Neupane, Z. Farhat, Wear and dent resistance of superelastic TiNi alloy, Wear 301 (1–2) (2013) 682–687, https://doi.org/10.1016/j.wear.2012.11.017.
[21] C. Miller, M. Zou, Microscale friction and deformation behavior of polydopamine/polytetrafluoroethylene-coated 60NiTi from nanoscratch tests, Thin Solid Films 743 (2022) 1–10, https://doi.org/10.1016/j.tsf.2021.139079. Art no. 139079.
[22] C. DellaCorte, NiTi alloys for tribological applications: the effects of serendipity on research and development, in: Presented at the Annual Postdoctoral Research and Career Symposium, October 6th. NASA/GRC-E-DAA-TN34568, Argonne IL, 2016 [Online]. Available: https://ntrs.nasa.gov/api/citations/20170003993/downloads/20170003993.pdf.
[23] S.K. Patel, A. Behera, Evolution of phases and their influence on shape memory effect by Varying Sintering parameters of NiTi alloys, Met. Mater. Int. 28 (11) (2022/11/01 2022) 2691–2705, https://doi.org/10.1007/s12540-021-01166-5.
[24] S. Bao, L. Zhang, H. Peng, Q. Fan, Y. Wen, Effects of heat treatment on martensitic transformation and wear resistance of as-cast 60NiTi alloy, Mater. Res. Express 6 (2019) 1–14, https://doi.org/10.1088/2053-1591/ab1b7a. Art no. 086573.
[25] O. Benafan, A. Garg, R.D. Noebe, H.D. Skorpenske, K. An, N. Schell, Deformation characteristics of the intermetallic alloy 60NiTi, Intermetallics 82 (2017) 40–52, https://doi.org/10.1016/j.intermet.2016.11.003.
[26] G. Tang, D. Zhang, J. Zhang, P. Lin, G. Dong, Self-recovery of worn surface of TiNi shape memory alloy, Appl. Surf. Sci. 321 (2014) 371–377, https://doi.org/10.1016/j.apsusc.2014.09.151.
[27] C. Miller, C. DellaCorte, M. Zou, Nanomechanical properties of hardened 60NiTi, Mater. Sci. Eng., A 800 (2021) 1–7, https://doi.org/10.1016/j.msea.2020.140284. Art no. 14028.
[28] L. Zhang, et al., Study on the corrosion behavior of NiTi shape memory alloys fabricated by electron beam melting, npj Mater. Degrad. 6 (1) (2022) 79, https://doi.org/10.1038/s41529-022-00289-3.
[29] C. DellaCorte, Novel super-elastic materials for advanced bearing applications, Adv. Sci. Technol. 89 (2014) 1–9 [Online]. Available: https://ntrs.nasa.gov/api/citations/20140010477/downloads/20140010477.pdf.
[30] A.C. Vieira, L.A. Rocha, N. Papageorgiou, S. Mischler, Mechanical and electrochemical deterioration mechanisms in the tribocorrosion of Al alloys in NaCl and in NaNO3 solutions, Corrosion Sci. 54 (2012) 26–35, https://doi.org/10.1016/j.corsci.2011.08.041.
[31] A.I. Muñoz, N. Espallargas, 5 - tribocorrosion mechanisms in sliding contacts, in: D. Landolt, S. Mischler (Eds.), Tribocorrosion of Passive Metals and Coatings, Woodhead Publishing, 2011, pp. 118–152, ch. 5.
[32] M.K. Stanford, Hot isostatic pressing of 60-Nitinol, NASA Tech. Rep. (2015). *NASA/TM-2015-218884*, https://www.techbriefs.com/component/content/article/tb/pub/briefs/manufacturing-prototyping/26497.
[33] M.-L. Li, W.-J. Gao, Y.-H. Zhou, Hot deformation behavior of 60NiTi shape-memory alloy fabricated by hot isostatic pressing, Mater. Res. Express 9 (1) (2022) 1–10, https://doi.org/10.1088/2053-1591/ac487e. Art no. 016511.
[34] ASTM G119-09, "Standard guide for determining synergism between wear and corrosion, in: " American Society for Testing and Materials. Book of Standards, 2021, pp. 1–6, https://doi.org/10.1520/G0119-09R22. *Developed by subcommittee G02.40*.
[35] ASTM G133-22, Standard test method for linearly reciprocating ball-on-flat sliding wear, in: American Society for Testing and Materials. Book of Standards, 2022, pp. 1–10, https://doi.org/10.1520/G0133-22. *Developed by subcommittee G02.40*.
[36] ASTM G3-14, Standard practice for conventions applicable to electrochemical measurements in corrosion testing, American Society for Testing and Materials. Book of standards (2019) 1–9, https://doi.org/10.1520/G0003-14R19. *Developed by subcommittee G01.11*.
[37] S.B. Arya, F.J. Joseph, Electrochemical methods in tribocorrosion, in: A. Siddaiah, R. Ramachandran, P.L. Menezes (Eds.), Tribocorrosion: Fundamentals, Methods, and Materials, Academic Press, 2021, pp. 43–77, 978-0-12-818916-0.
[38] G.A. Rodríguez-Bravo, M. Vite-Torres, J.G. Godínez-Salcedo, Corrosion rate and wear mechanisms comparison for AISI 410 stainles steel exposed to pure corrosion and abrasion-corrosion in a simulated marine environment, Tribology in Industry 41 (3) (2019) 394–400, https://doi.org/10.24874/ti.2019.41.03.09.
[39] K. Khanlari, M. Ramezani, P. Kelly, M. Hayat, P. Cao, T. Neitzert, An investigation on microstructural and mechanical properties of porous 60NiTi parts solutionized by different cost-effective methods, Metallography, Microstructure & Analysis 7 (3) (2018) 334–346, https://doi.org/10.1007/s13632-018-0443-4.
[40] K. Khanlari, M. Ramezani, P. Kelly, P. Cao, T. Neitzert, Mechanical and microstructural characteristics of as-sintered and solutionized porous 60NiTi, Intermetallics 100 (2018) 32–43, https://doi.org/10.1016/j.intermet.2018.06.001.
[41] Z. Du, Z. Hu, Y. Feng, F. Mo, The effect of powder composition on the microstructure and corrosion resistance of laser cladding 60NiTi alloy coatings on SS 316L, Metals 11 (7) (2021) 1–16, https://doi.org/10.3390/met11071104. Art no. 1104.

[42] K. Khanlari, M. Ramezani, P. Kelly, P. Cao, T. Neitzert, An investigation on reasons causing inferiority in unlubricated sliding wear performance of 60NiTi as compared to 440c steel, Tribol. Trans. 62 (1) (2019) 96–109, https://doi.org/10.1080/10402004.2018.1516326.
[43] K. Khanlari, M. Ramezani, P. Kelly, P. Cao, T. Neitzert, Comparison of the reciprocating sliding wear of 58Ni39Ti-3Hf alloy and baseline 60NiTi, Wear 408–409 (2018) 120–130, https://doi.org/10.1016/j.wear.2018.05.011.
[44] Y. Yan, A. Neville, Bio-tribocorrosion: surface interactions in total joint replacement (TJR), in: Y. Yan (Ed.), Bio-tribocorrosion in Biomaterials and Medical Implants, Elsevier, 2013, pp. 309–340.
[45] Z. Yi, et al., Interfacial friction at action: interactions, regulation, and applications, Friction (2023/03/13 2023) 1–28, https://doi.org/10.1007/s40544-022-0702-x.
[46] Q. Zeng, G. Dong, Influence of load and sliding speed on super-low friction of NiTiNOL 60 alloy under castor oil lubrication, Tribol. Lett. 52 (1) (2013) 47–55, https://doi.org/10.1007/s11249-013-0191-1.
[47] R. Neupane, Z. Farhat, Wear mechanisms of NiTinol under reciprocating sliding contact, Wear 315 (1–2) (2014) 25–30, https://doi.org/10.1016/j.wear.2014.02.018.
[48] C.-O.A. Olsson, A.N.I. Munoz, S. Cao, S. Mischler, Modeling current transients in a reciprocal motion tribocorrosion experiment, J. Electrochem. Soc. 168 (3) (2021/03/02 2021), 031503, https://doi.org/10.1149/1945-7111/abe6ed. Art no.
[49] E. Ghali, Corrosion Resistance of Aluminum and Magnesium Alloys: Understanding, Performance, and Testing (Wiley Series in corrosion.). Hoboken, New Jersey, John Wiley & Sons Inc., Hoboken, New Jersey, 2010, 978-0-471-71576-4 (in English).
[50] D. Landolt, S. Mischler, M. Stemp, S. Barril, Third body effects and material fluxes in tribocorrosion systems involving a sliding contact, Wear 256 (5) (2004/03/01/2004) 517–524, https://doi.org/10.1016/S0043-1648(03)00561-1.
[51] C. Yan, Q. Zeng, Y. Xu, W. He, Microstructure, phase and tribocorrosion behavior of 60NiTi alloy, Appl. Surf. Sci. 498 (2019) 1–10, https://doi.org/10.1016/j.apsusc.2019.143838. Art no. 143838.
[52] J. Yang, Y. Song, K. Dong, E.-H. Han, Research progress on the corrosion behavior of titanium alloys, Corrosion Rev. 41 (1) (2023) 5–20, https://doi.org/10.1515/correv-2022-0031.
[53] P. Renner, Y. Chen, Z. Huang, A. Raut, H. Liang, Tribocorrosion influenced pitting of a duplex stainless steel, Lubricants 9 (5) (2021) 1–11, https://doi.org/10.3390/lubricants9050052.
[54] H. Wang, et al., Corrosion behavior of NiTi alloy subjected to femtosecond laser shock peening without protective coating in air environment, Appl. Surf. Sci. 501 (2020), https://doi.org/10.1016/j.apsusc.2019.144338. Art no. 144338.
[55] K. Khanlari, M. Ramezani, P. Kelly, P. Cao, T. Neitzert, Reciprocating sliding wear behavior of 60NiTi as compared to 440C steel under lubricated and unlubricated conditions, Tribol. Trans. 61 (6) (2018) 991–1002, https://doi.org/10.1080/10402004.2018.1460434.
[56] M.K. Stanford, in: Hardness and Microstructure of Binary and Ternary Nitinol Compounds," in "NASA Technical Report," National Aeronautics and Space Administration, Glenn Research Center, No. GRC-E-DAA-TN73728, 2016 issue NASA/TM-2016-218946. [Online]. Available: https://ntrs.nasa.gov/citations/20160001689.
[57] G.X. Xu, L.J. Zheng, F.X. Zhang, H. Zhang, Influence of solution heat treatment on the microstructural evolution and mechanical behavior of 60NiTi, J. Alloys Compd. 775 (2019) 698–706, https://doi.org/10.1016/j.jallcom.2018.10.015.
[58] C. Yan, Q. Zeng, W. He, J. Zhu, Enhanced surface hardness and tribocorrosion performance of 60NiTi by boron ion implantation and post-annealing, Tribol. Int. 155 (2021) 1–11, https://doi.org/10.1016/j.triboint.2020.106816. Art no. 106816.
[59] M. Venkatesh, R. Salloom, A.V.M. Rao, A.V. Aditya, Tribocorrosion mechanisms in sliding contacts, in: A. Siddaiah, R. Ramachandran, P.L. Menezes (Eds.), Tribocorrosion: Fundamentals, Methods, and Materials, Academic Press, 2021, pp. 79–91, 978-0-12-818916-0.
[60] S. Mischler, S. Debaud, D. Landolt, Wear-accelerated corrosion of passive metals in tribocorrosion systems, J. Electrochem. Soc. 145 (3) (1998) 750–758, https://doi.org/10.1149/1.1838341.
[61] A. López-Ortega, R. Bayón, J.L. Arana, Evaluation of protective coatings for offshore applications. Corrosion and tribocorrosion behavior in synthetic seawater, Surf. Coat. Technol. 349 (2018) 1083–1097, https://doi.org/10.1016/j.surfcoat.2018.06.089.
[62] A. Ghanbarzadeh, F.M. Salehi, M. Bryant, A. Neville, A new asperity-scale mechanistic model of tribocorrosive wear: synergistic effects of mechanical wear and corrosion, J. Tribol. 141 (2) (2019) 1–12, https://doi.org/10.1115/1.4041246.